Atomic short-range order and incipient long-range order in high-entropy alloys

Prashant Singh, A. V. Smirnov, and D. D. Johnson

Phys. Rev. B **91**, 224204 — Published 29 June 2015

DOI: 10.1103/PhysRevB.91.224204

Atomic Short-Range Order and Incipient Long-Range Order in High-Entropy Alloys

Prashant Singh,[1,*] A. V. Smirnov,[1,†] and D. D. Johnson[1,2,‡]

[1] *Ames Laboratory, U.S. Department of Energy, Iowa State University, Ames, Iowa 50011-3020, USA*

[2] *Materials Science & Engineering, Iowa State University, Ames, Iowa 50011-2300, USA*

(Dated: June 10, 2015)

Within density-functional theory, we apply an electronic-structure-based thermodynamic theory to calculate short-ranged order (SRO) in homogeneously disordered substitutional N-component alloys, and its electronic origin. Using the geometric properties of an (N-1)-simplex that describes the Gibbs (compositional) space, we derive the analytic transform of the SRO eigenvectors that provides a unique description of high-temperature SRO in N-component alloys and the incipient low-temperature long-range order. We apply the electronic-based thermodynamic theory and the new general analysis to ternaries (A1 Cu-Ni-Zn and A2 Nb-Al-Ti) for validation, and then to quinary Al-Co-Cr-Fe-Ni high-entropy alloys for predictive assessment.

PACS numbers: 61.66.Dk, 63.20.dk, 63.50.Gh, 75.40.-s, 64.75.Nx, 71.23.-k, 71.20.Be

I. INTRODUCTION

Multicomponent metallic alloys constitute an important, widely used class of technological materials. Properties of N-component alloys are sensitive to the state of chemical order in a stable lattice structure. Recently, so-called high-entropy alloys (HEA) have drawn much attention due to their remarkable properties. HEA consists of five or more ($N \geq 5$) elements with (nearly) equal composition of atomic species. If not too large, their alloy formation enthalpy ΔE_f, dictating ordering ($\Delta E_f < 0$) or phase-segregation ($\Delta E_f > 0$), are easily overcome by the large entropy associated with near-equiatomic compositions, stabilizing solid-solutions and suppressing the formation of (small unit cell) intermetallic phases.[1,2]

While solid solutions lack chemical long-range order (LRO), they often possess atomic short-range order (SRO) that reveal the high-temperature, incipient chemical ordering tendency, either clustering or ordering. Often the SRO is indicative of the low-temperature LRO, albeit not guaranteed for first-order transitions. For a stoichiometric N-component alloy, in general, there must be $N-1$ ordering transitions from the homogeneous phase. Hence, SRO can often be used to predict the expected LRO.[3,4]

Notably, SRO can be measured in diffuse-scattering (x-ray, electron and neutron) experiments by extracting Warren-Cowley SRO parameters,[5–7] $\alpha_{\mu\nu}(\mathbf{k})$ at scattering wavevector $\mathbf{k}$, which are normalized pair (correlation) probabilities discussed later. For multicomponent alloys, diffuse scattering intensities are given in terms of Laue units,[3,4,8,9] i.e., $c_\mu(\delta_{\mu\nu} - c_\nu)\,[f_\mu - f_\nu]^2$, by

$$I(\mathbf{k}) = \sum_{\mu,\nu} c_\mu(\delta_{\mu\nu} - c_\nu)\,[f_\mu - f_\nu]^2\,\alpha_{\mu\nu}(\mathbf{k}) \ , \qquad (1)$$

with atomic scattering form factors f_μ, component labels (μ, Greek lower-case letters), and compositions c_μ. Only off-diagonal SRO parameters may be measured if there is contrast, i.e., $f_\mu - f_\nu \neq 0$. For the well-studied A-B binaries, a single $\alpha_{AB}(\mathbf{k})$ correlation can be observed, and diagonal values are obtained via sum rules dictated by the optical theorem. Interpretation is straightforward: If not an A atom, then a B atom in a favorable wavevector ordering sequence. For N-component alloys, $N(N-1)/2$ pairs must be measured, achieved only if there is sufficient scattering $f_\mu - f_\nu$ contrast; but, without all the off-diagonal pairs, the SRO cannot be interpreted.

Here, we do not address the challenge of how one measures all off-diagonal pairs of N-component alloy. We provide a general theoretical method to predict all pair correlations and, in particular, how to interpret uniquely the SRO manifest in $\alpha_{\mu\nu}(\mathbf{k})$. The approach uses the KKR Green's function electronic-structure method in combination with an inhomogeneous coherent-potential approximation (CPA) developed for binaries[10,11] and extended to ternaries.[3,8,12] From the KKR-CPA, we may connect SRO to its electronic origin (competing effects of band-filling, hybridization, Fermi-surface nesting, van Hove states, ...), and confirm the behavior by direct calculation of formation energies ΔE_f for partially ordered states.

After some background, we relate in section III the SRO to second-order (infinitesimal) concentration variations to the alloy free-energy (chemical *stability matrix*). Eigenvectors of the stability matrix reveal the incipient order reflected in the SRO. Describing the N-component system in Gibbs space as an $(N-1)$-simplex using $\{c_\mu\}$ as natural barycentric coordinates, we establish the transform in Gibbs space that yields a correct analysis of SRO in N-component solid solutions. In particular, we obtained the transform's matrix elements analytically for N-dimensions that guarantees the SRO eigenvectors are properly chemically and geometrically orthogonal. We apply the new SRO analysis to two well-studied ternaries (A1 Cu-Ni-Zn[3,8] and A2 Nb-Al-Ti[12]) to validate, and then to quinary Al-Co-Cr-Fe-Ni alloys. With this general analysis approach, our electronic-structure-based SRO theory can be analyzed using the SRO eigenvectors in a concentration-wave (Fourier) analysis,[3,8,13] now rigorously generalized to N-components alloys.

II. BACKGROUND

The study of SRO in disordered solid-solutions has a long history, mostly on binaries and a few ternaries. In the multicomponent case, the complexity with experiments and interpretation of the pair correlations remains a challenge. In disordered solid-solution alloys, the SRO is thermally induced infinitesimal concentration fluctuation and directly related to the chemical pair correlations.[8,9,13–16] In terms of site (i and j) occupation variables, pair correlations $\mathrm{q}^{ij}_{\mu\nu}(\mathbf{k})$ are mathematically defined as

$$q^{ij}_{\mu\nu}(\mathbf{k}) = \langle(\xi^i_\mu - c^i_\mu)(\xi^i_\nu - c^i_\nu)\rangle = \langle\xi^i_\mu\xi^j_\nu\rangle - \langle\xi^i_\mu\rangle\langle\xi^j_\nu\rangle, \quad (2)$$

where $\langle ...\rangle$ represents a thermodynamic average, and ξ^i_μ is a site-occupation variable; that is, $\xi^i_\mu = 1(0)$ if the site is (is not) occupied by an μ-type atom at the site i, hence, $\langle\xi^i_\mu\rangle = c^i_\mu$. For an N-component alloy in a "host" picture, there are N-1 independent fluctuations, as the host (dependent) variable is dictated by a site single-occupancy constraint, i.e., $\sum_\mu \xi^i_\mu = 1$, forcing $\sum_\mu c^i_\mu = 1$, so there is only $\mathrm{N}-1$ independent occupations. Notably, a vacancy can be treated as just another independent species (not host). With ξ^i_μ idempotent ($(\xi^i_\mu)^2 = \xi^i_\mu$), site-diagonal pair correlations $\langle\xi^i_\mu\xi^i_\nu\rangle$ obey the sum rule

$$q^{ii}_{\mu\nu}(\mathbf{k}) = c^i_\mu(\delta_{\mu\nu} - c^i_\nu) \quad (3)$$

where $\delta_{\mu\nu}$ is Kronecker delta function over species. For an A-B binary, $\mathrm{c_A} + \mathrm{c_B} = 1$, and, if $\mathrm{c_A}$ is considered independent, then $\mathrm{c_B}$ is the dependent (host) variable, and $\mathrm{q^{ii}_{AA}} = \mathrm{c_A}(1 - \mathrm{c_A})$.

We now can define Warren-Cowley (WC) parameters[5–7] as normalized pair probabilities in Laue units, i.e.,

$$\alpha^{ij}_{\mu\nu}(\mathbf{k}) = \frac{q^{ij}_{\mu\nu}(\mathbf{k})}{c_\mu(\delta_{\mu\nu} - c_\nu)} \quad (4)$$

and in real space this can be understood in terms of pair probabilities: $\mathrm{p}^{ij}_{\mu\nu} = c^i_\mu c^j_\nu\left[1 - \alpha^{ij}_{\mu\nu}\right]$, where point probabilities are the concentrations. For example, if $\alpha \to 0$, then pair correlation vanishes; while for $\alpha < 0$ ($\alpha > 0$) system correlations reflect ordering (clustering).

Experiments only can measure the off-diagonal pair correlations (SRO) defined in Eqs. 1 or 2. Through the conservation of probability (optical theorem) it is straightforward to derive this sum rule[9,16]

$$\sum_\nu c^j_\nu \alpha^{ij}_{\mu\nu} = 0 \quad (5)$$

that allows us to get unmeasured (diagonal) correlations. As shown rigorously elsewhere,[9] the theory for SRO for disordered alloys used here calculates the non-singular $(\mathrm{N}-1)\times(\mathrm{N}-1)$ portion of inverse of

$$\left[q^{-1}(\mathbf{k})\right]_{\mu\nu} = \left[\frac{\delta_{\mu\nu}}{c_\mu} + \frac{1}{c_N}\right] - \beta S^{(2)}_{\mu\nu}(\mathbf{k}) \quad (6)$$

where $\{\mu,\nu\} \in 1, \mathrm{N}-1$ and β is $(\mathrm{k_B T})^{-1}$, defined by temperature (T) and Boltzman constant ($\mathrm{k_B}$). The expression is exact.[9,17,18] Most notably, $\mathrm{S}^{(2)}(\mathbf{k})$ – the chemical fluctuation stability matrix – is a thermodynamic functional that reflects the free-energy cost of a pair fluctuation, and is represented by a symmetric matrix; importantly, it is not a pair interaction, as often assumed.[9] At the spinodal temperature, $\mathrm{T_{sp}}$, for a specific maximum wavevector instability, the inverse pair correlation first vanishes (i.e., the pair correlation diverge). Hence, from the stability matrix we can determine which wavevector instability first goes unstable, what pair(s) drive this instability, and at what temperature this instability occurs. All this information is useful for predicting and characterizing SRO in any complex solid-solution, like any HEA.

From linear-response theory, $\mathrm{S}^{(2)}_{\mu\nu}(\mathbf{k})$ is the second-variation of the alloy Grand Potential with respect to composition fluctuations, evaluated in the high-T disordered phase.[4,9] That is, expanding the interacting electronic part of the free-energy in a functional Taylor's series relative to the disordered alloy, we find[9,10,18–20] that

$$\begin{aligned}\Delta F(\{c^i_\mu\}) &= F(\{c^i_\mu\}) - F(\{\bar{c}_\mu\}) \\ &= \frac{1}{2}\sum_{\mu\nu,ij}\Delta c^{\dagger i}_\mu \frac{\delta^2 F}{\delta c^{\dagger i}_\mu \delta c^j_\nu}|_{\{c_\mu\}}\Delta c^j_\nu \\ &\approx \frac{1}{2}\sum_{\mu\nu}\int_{BZ} d\mathbf{k}\ \Delta c^\dagger_\mu(\mathbf{k}) S^{(2)}_{\mu\nu}(\mathbf{k})\Delta c_\nu(\mathbf{k}), \quad (7)\end{aligned}$$

and where the first variation is zero by symmetry of the disordered state. The Brilliouin zone (BZ) integral is over that of the solid-solution's Bravais lattice, where the fluctuations $\mathrm{c^i_\mu} - \bar{\mathrm{c}}_\mu$ (i.e., Fourier wave $\Delta\mathrm{c}_\mu(\mathbf{k})$) happen. The total alloy free energy, $\mathrm{F} = F_0 + F_{int}$, can be written as the sum of non-interacting, $\mathrm{F_0}$, and interacting, $\mathrm{F_{int}}$, contributions, where $\mathrm{F_0}$ is related to point entropy (S_{pt}) [i.e., $\mathrm{TS}_{pt} = -\mathrm{k_B T}\sum \mathrm{c^i_\mu} ln \mathrm{c^i_\mu}$] and $\mathrm{F_{int}}$ comes from electronic structure (ion-ion, band-energy, double-counting and exchange-correlation). $\mathrm{S}^{(2)}_{\mu\nu}(\mathbf{k})$ is determined from $\mathrm{F_{int}}$ in the solid-solution phase, and encompasses all electronic effects (hybridization, band-filling, Fermi-surface nesting, van Hove states, ...).

If evaluated in the homogeneous state, $\alpha_{\mu\nu}(\mathbf{k})$ is an approximation to the state with actual SRO, and it can be calculated with KKR-CPA linear-response codes.[3,4,12] Given calculations of (6), the Warren-Cowley SRO parameters[5–7] are determined from (4). What remains to be determined is ordering fluctuations embodied in $\mathrm{S}^{(2)}_{\mu\nu}(\mathbf{k})$.

III. CHEMICAL SRO EIGENVECTORS

In an N-component alloy with $\sum_{\mu=1}^{N} \mathrm{c^i_\mu} = 1$, the independent compositional fluctuations are described by $\mathrm{N}-1$ component vectors. The associated Gibbs space is

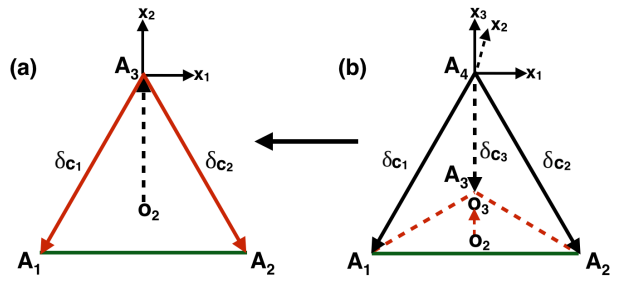

FIG. 1. (color online) Gibbs space for (a) ternary shown by an equilateral triangle (2-simplex) and (b) quaternary shown by a regular tetrahedron (3-simplex), where $\{\delta c_i\}$ are the directions of concentrations fluctuations. Barycentric points 'o_2' and 'o_3' are centroids of 2- and 3-simplex, respectively and $\{x_i\}$ are Cartesian labels.

N-dimensional, and represented by $(N-1)$-simplices: for N=2, a line (1-simplex), for N=3, a triangle (2-simplex), for N=4, a tetrahedron (3-simplex), and so on. From sum rules, $\{c_\mu\}$ are natural barycentric coordinates as developed for finite-element methods,[21] and define coordinates in whole Gibbs space. Figure 1 shows a schematic for ternary and quaternary simplices and arrows labelled by δc_μ's are the directions of fluctuations in Gibbs space (parallel to directions of increasing concentrations); generally, these axes are oblique to one another – not geometrically orthogonal.[3,9,22,23]

The fluctuation energy (in matrix-vector notation) is

$$\Delta F = \hat{c}^\dagger S \hat{c} \tag{8}$$

$$= \hat{x}^\dagger (T^\dagger S T)\hat{x} = \hat{x}^\dagger \hat{S} \hat{x}, \tag{9}$$

By solving the characteristic equation for (8), the $S_{\mu\nu}(\mathbf{k})$ eigenvectors (e_N) exhibit a *host dependence*, and possibly unphysical (negative) concentrations. Formally, it is first necessary to transform from Gibbs ($\hat{c}$) to a Cartesian ($\hat{x}$) coordinate system ($\hat{c} = T\hat{x}$), where $\hat{S} = T^\dagger S T$ in (9) has eigenvectors (e_X) that are now *host independent* but represented in Cartesian space. Then, we must transform e_X back to Gibbs space ($\mathbf{e}_G = T\mathbf{e}_X$) to get the physically proper eigenmodes and concentrations (ordering probabilities). Because compositional representation of Gibbs space based on simplices is oblique, the transformation matrix T is not unitary, i.e., $T^{-1} \neq T^\dagger$ and $TT^\dagger \neq 1$, so eigenvectors e_X are not same as e_G, which are the correct ones in Gibbs space. Notably, with T known analytically for the N-dimensional case, we may analyze all SRO directly via e_G.

A. Matrix elements of T analytically for N-component alloys

The form of T is well known in terms of barycentric coordinates for N-dimensions; typically the matrix elements and inverse transformations are then numerically calculated. Remarkably, however, we can analytically derive the matrix elements of T for N-dimensional Gibbs ("equilateral") simplices (see Appendix). With T known analytically, we may obtain e_G from measured $\alpha_{\mu\nu}(\mathbf{k})$ or calculated $S_{\mu\nu}(\mathbf{k})$ for the N-component solid solution.

The Jacobian transformation from Cartesian to oblique coordinates is well-known for any dimension, i.e., T is

$$^{N\text{-}1}T = \begin{pmatrix} x_1^1 - x_1^N & x_1^2 - x_1^N & \cdots & x_1^{N-1} - x_1^N \\ x_2^1 - x_2^N & x_2^3 - x_2^N & \cdots & x_2^{N-1} - x_2^N \\ \cdots & \cdots & \cdots & \cdots \\ \cdots & \cdots & \cdots & \cdots \\ x_{N-1}^1 - x_N^N & x_{N-1}^2 - x_N^N & \cdots & x_{N-1}^{N-1} - x_N^N \end{pmatrix} \tag{10}$$

where $\{X_j^i\}$ represents coordinates of j^{th} vertex relative to the host vertex $\{X_j^N\}$. In a host picture, the N^{th} vertex in $(N-1)$-simplex is redundant from the sum rule for barycentric coordinates so the T matrix will always be rank $N-1$. Coordinates of all $(N-1)$ vertices for Gibbs simplices are derived (Appendix) as

$$X_i^j - X_i^N = -\frac{1}{X_i^i}\sqrt{\frac{2(N-1)}{N}}\left[\mathbf{X}_{i-1}^i \cdot \mathbf{X}_{i-1}^j + \frac{1}{N-1}\right] \tag{11}$$

and each i, j runs from 1 to $N-1$.

From this analytic matrix element for T for any Gibbs space, we may evaluated easily the specific ternary and quinary cases addressed in results section. For a ternary (2-simplex), the 2×2 ^2T matrix is

$$^2T = \begin{pmatrix} -1 & -1/\sqrt{3} \\ 1 & -1/\sqrt{3} \end{pmatrix}, \tag{12}$$

while, for quinary(4-simplex), the 4×4 ^4T matrix is

$$^4T = \begin{pmatrix} -1 & -1/\sqrt{3} & -1/\sqrt{6} & -1/\sqrt{10} \\ 1 & -1/\sqrt{3} & -1/\sqrt{6} & -1/\sqrt{10} \\ 0 & 2/\sqrt{3} & -1/\sqrt{6} & -1/\sqrt{10} \\ 0 & 0 & \sqrt{3/2} & -1/\sqrt{10} \end{pmatrix}. \tag{13}$$

Notice that ^2T (ternary) is a submatrix of ^4T (quinary), and so too is ^3T the 3×3 submatrix (quaternary).

B. Concentration Waves in N-component Alloys

Given $\mathbf{e}_G$ (ordering normal modes) and T (transform matrix), we need to interpret the order reflected in the SRO, accomplished best by Fourier analysis. The occupational vector, $\hat{n}(\mathbf{r})$, give the probabilities of an atom to occupy specific sites in a crystal structure. In substitutional solid-solutions, $n_i(\mathbf{r})$ is identical to concentrations, $c_i(\mathbf{r})$. But, in ordered phases, this depends on the type of order and real-space site coordinates.[13] The vector $\hat{n}(\mathbf{r})$ for a N-component alloy, where all sites are represented by the same Bravais lattice, can be expanded in a Fourier series (concentration wave) and written in terms of nor-

mal modes as

$$\begin{bmatrix} n^1(\mathbf{r}) \\ n^2(\mathbf{r}) \\ \vdots \\ n^{N-1}(\mathbf{r}) \end{bmatrix} = \begin{bmatrix} c^1(\mathbf{r}) \\ c^2(\mathbf{r}) \\ \vdots \\ c^{N-1}(\mathbf{r}) \end{bmatrix} + \sum_{s,\sigma} \eta^s_\sigma \begin{bmatrix} \nu^1_\sigma(\mathbf{k}_s) \\ \nu^2_\sigma(\mathbf{k}_s) \\ \vdots \\ \nu^{N-1}_\sigma(\mathbf{k}_s) \end{bmatrix} \times \sum_{j_s} \gamma_\sigma(\mathbf{k}_{j_s}) e^{i\mathbf{k}_{j_s}\cdot\mathbf{r}}. \quad (14)$$

For a given crystal lattice vector $\mathbf{r}$, $\mathrm{c^{N-1}}(\mathbf{r})$ is composition of the $(\mathrm{N}-1)^{th}$ component. The sums run over the star s (inequivalent wavevectors that define ordering), σ (eigenvector branch of the free-energy quadric), and j_s (equivalent wavevectors in the s^{th} star). The other quantities are: LRO parameter η^{s}_σ for the σ^{th} branch and s-star; $\nu^{\mathrm{N-1}}_\sigma$ is $(\mathrm{N}-1)$-component vector of the normal concentration mode ($\mathrm{e_G}$) of $\mathrm{S}_{\mu\nu}(\mathbf{k})$ for the σ^{th} branch; and the symmetry coefficient $\gamma_\sigma(\mathbf{k}_{\mathrm{j_s}})$ determined by normalization condition and geometry.

IV. COMPUTATIONAL DETAILS

We use a Korringa-Kohn-Rostoker (KKR) Coherent Potential Approximation (CPA) code.[24–26] For metallic solid-solutions, the screened-CPA is used to incorporate Friedel screening from charge correlations in the local chemical environment.[26] As our KKR-CPA-based SRO theory is only coded for the Atomic Sphere Approximation (ASA), we use the KKR-CPA-ASA for all results, and include so-called muffin-tin (MT) corrections to the ASA total energies. We also evaluate electronic properties and total energies using Voronoi polyhedra (VP) integration[27] for spherically averaged radial functions in the site-centered, spherical-harmonic ($\mathrm{Y_L}$) basis. We include *s-, p-, d-* and *f*-symmetries in the KKR basis, i.e., truncated at $\mathrm{L_{max}}$=3, where $\mathrm{L} \equiv (\mathrm{l,m})$.

Potentials, charge densities, and total energies are obtained using a complex-energy Gauss–Legendre semicircular contour with 24 points, and Brillioun zone integrations use special k-point method[28] with a $20 \times 20 \times 20$ mesh. We use the von-Barth–Hedin[29] local density approximation as parameterized by Moruzzi, Janak and Williams.[30] Self-consistency for potentials and charge densities is achieved with convergence technique based on modified Broyden's second method.[33] Scalar-relativistic effects are included, but spin-orbit is ignored. Because the potential zero $\mathrm{v_0}$, i.e., *muffin-tin zero*, can dramatically affect stability prediction for spherical potentials, we use a variational definition[32] that yields kinetic energies that approach those of full-potential methods.[31,32]

The first-principles theory of SRO in multicomponent alloys has been presented before.[10,11,20] The complete expression for $S^{(2)}_{\mu\nu}(\mathbf{k};\mathrm{T})$, one that includes all electronic-structure, charge screening and transfer, has been derived only for binaries.[10,11,20] The importance of metallic screening for SRO calculation in the solid solution phase has been discussed before for binaries.[34] However, at fixed composition, assuming site charges change little with SRO, Pettifor's force theorem can be applied and $S^{(2)}_{\mu\nu}(\mathbf{k};\mathrm{T})$ then has contributions only from the band-energy variations.[3,8] Hence, for present purpose to showcase the prediction and interpretation of SRO for N-component metallic solid-solutions, we calculate all $S^{(2)}_{\mu\nu}(\mathbf{k};\mathrm{T})$ results using the *band-energy-only* expression; that is, double counting terms and exchange correlation are neglected by invoking the force theorem. (We will add these variations in the future.) The scalar-relativistic KKR-CPA-ASA potentials, charge densities, and scattering matrices for a given solid-solution are used to then evaluate the linear-response expression for $S^{(2)}_{\mu\nu}(\mathbf{k};\mathrm{T})$. The expression for $S^{(2)}_{\mu\nu}(\mathbf{k};\mathrm{T})$ are evaluated on a log-mesh along the Matsubara poles, and interpolated to the correct poles (temperature) for use in response functions.[10,11]

Thermodynamically, the Warren-Cowley parameters (4)[5–7] must obey the optical theorem and conserve the particle number associated with the through beam, i.e., at the i^{th} site (see Review [9])

$$\alpha^{ii}_{\mu\nu} = 1 - \frac{\delta_{\mu\nu}}{c_{\nu i}} = \frac{1}{V_{BZ}} \int d\mathbf{k}\ \alpha_{\mu\nu}(\mathbf{k}). \quad (15)$$

Any mean-field approximation to $\mathrm{S^{(2)}}(\mathbf{k},\mathrm{T})$ does not guarantee this sum rule,[9] as is true of the CPA. As shown from (6), modifying $S^{(2)}_{\mu\nu}(\mathbf{k},\mathrm{T}) \equiv \mathrm{S}^{(2)MF}_{\mu\nu}(\mathbf{k},\mathrm{T}) - \Lambda_{\mu\nu}(\mathrm{T})$ satisfied the sum rule[8–10] with

$$\Lambda_{\mu\nu}(T) = \frac{1}{V_{BZ}} \sum_\beta \int d\mathbf{k}\ S^{(2)MF}_{\mu\beta}(\mathbf{k},T)\alpha_{\beta\nu}(\mathbf{k}). \quad (16)$$

This coupled set of equations may be solved by Newton-Raphson techniques, using multi-dimensional mapping for inversion of tensors. $S^{(2)}(\mathbf{k},\mathrm{T})$ is typically very weakly temperature dependent arising from the Fermi factors (see below), while $\alpha_{\mu\nu}(\mathbf{k})$ strongly depends on temperature, diverging at $\mathrm{T_{sp}}$, see (6). The correction is historically called the Onsager cavity field correction,[35] which renormalizes the thermodynamic excitation energies to conserve the diffuse intensity over the Brilliouin zone. Although not commonly used as a more proper mean-field theory, this single-site fix to mean-field theory corrects the topological error in mean-field phase diagrams, such as Bragg-Williams (Ising) models.[36]

Besides energy- and species-dependent matrix elements $\mathrm{M^{LL'}_{\mu\nu}}(\epsilon)$ and Fermi factors $f(\epsilon)$, $\mathrm{S^{(2)}}(\mathbf{k},\mathrm{T})$ is found from the KKR scattering path operator, $\tau_{\mathrm{LL'}}(\mathbf{k};\epsilon)$, which determines the Green's function and embodies all electronic-structure effects.[3,8,10,11] In brief, $\mathrm{S^{(2)}}(\mathbf{k},\mathrm{T})$ is a generalized susceptibility, and, roughly,[18] in terms of the Bloch spectral functions $\mathrm{A}(\mathbf{k};\epsilon) = -\Im\tau(\mathbf{k};\epsilon)/\pi$ (dis-

persion), we may suggestively write it as

$$S^{(2)}_{\mu\nu}(\mathbf{q};T) \sim \int d\epsilon\ M_{\mu\nu}(\epsilon) \int d\epsilon' \left[\frac{f(\epsilon;T)-f(\epsilon';T)}{\epsilon-\epsilon'}\right] \times \frac{1}{\Omega_{BZ}} \int\ d\mathbf{k}\ A(\mathbf{k};\epsilon)A(\mathbf{k}+\mathbf{q};\epsilon') \quad (17)$$

All valence states contribute to (17). If only hole and electron states near the Fermi energy, $\mathrm{E_F}$, dominate, the bracketed [...] term collapses the energy integrals to

$$S^{(2)}(\mathbf{q};T) \to \int\ d\mathbf{k}\ A(\mathbf{k};E_F)A(\mathbf{k}+\mathbf{q};E_F), \quad (18)$$

a convolution integral of the Fermi surface states and the origin for so-called Fermi-surface "nesting".[3,8,18] Due to alloying, even in a metallic system, hybridized states well below $\mathrm{E_F}$ in (17) can drive ordering, as for NiPt,[37] or van Hove features at $\mathrm{E_F}$ contribute, as for CuPt.[38] In short, the nature and electronic origin of the SRO may be determined directly.

For completeness, using a laptop computer with an Intel i7 (2.3 GHz quad core) processor, we provide some timings involved in evaluating the self-consistent potentials and linear-response $\mathrm{S^{(2)}}(\mathbf{q};E)$ for 24 energy points on the semi-circular or Matsubara contour. For pure bulk (one-atom) elemental groundstates, KKR-CPA SCF calculations require 10-20 iteration with ∼10 seconds per iteration. However, for bulk solid-solutions (effectively 1-atom cells for A1 or A2), KKR-CPA SCF calculations require 30-50 iteration with ∼25-50 seconds per iteration, due to cost of the CPA convergence that often takes longer than charge convergence. Typically, as the number of components (disorder) increases, the CPA is easier to converge and uses fewer iterations. For linear-response calculations in serial mode for a binary, the $\mathrm{S^{(2)}}(\mathbf{q};E)$ requires ∼3600 seconds. Post-processing analysis requires another ∼20 seconds. For the N-component case, the time grows linearly with N-1 due to extra matrix elements in $\mathrm{S^{(2)}}$. For magnetic case in local-spin density approximation, the timings are double that of non-magnetic case due to calculating both the majority and minority spin channels. If the linear-response is done for all 24 energies in parallel (not a laptop), divide the time by 24, or ∼150 seconds. Of course, structural minimization of lattice constants can be done to get the minimum-energy potentials, or use the experimental lattice constants, and those potentials are then used for SRO predictions.

So, it is now possible both to *predict* SRO from the electronic structure and to *interpret* the SRO correctly by extracting the proper eigenvectors of $\mathrm{S^{(2)}}(\mathbf{k},\mathrm{T})$ for arbitrary N-component alloys.

V. RESULTS

The prediction and characterization of chemical ordering instabilities in multicomponent alloys is of great practical and fundamental interest. The temperature-dependent chemical order is determined by the balance between ordering energy (favoring long-range order) and entropy (favoring disorder). The ordering energy largely reflects the underlying electronic effects within the disordered alloy. We have divided this section into two parts, first validation of updated $\mathrm{S^{(2)}}(\mathbf{k})$ code and new generalized transformation approach to interpret SRO eigenvectors using well-studied binary and ternary systems, and the second focuses on analysis of high-entropy alloy candidate Al-Co-Cr-Fe-Ni quinary system. We report k-space wavevectors in units of $2\pi/a$ and real-space site coordinates in units of a. We calculate the KKR-CPA formation energy for a solid solution in a phase x (e.g., A1, A2, or A3) as $\Delta E^x_f(V) = E^x(V) - \sum_\alpha c_\alpha E^o_\alpha(V^o_\alpha)$, where the $E^o_\alpha(V^o_\alpha)$ is the energy of the alloying element in its ground-state phase and equilibrium volume. As discussed by Alam et al.,[39] formation energy provides a good estimate of miscibility gap ($\mathrm{T_c} = \Delta\mathrm{E_f}/S_{pt}$) and order-disorder temperature ($\mathrm{T_c} = \Delta\mathrm{E_f}/\mathrm{k_B}$), where there is a cancellation in entropy to second-order from above and just below the transition at fixed concentration.[39]

A. Validation and Example Analysis

We first validate our updated $\mathrm{S^{(2)}_{\mu\nu}}(\mathbf{k};\mathrm{T})$ calculations and new generalized SRO analysis by investigating a clustering binary and two ordering ternaries to show previous calculations and experiments are reproduced quantitatively.

A1 $\mathbf{Cu_{50}Ni_{50}}$ – Diffuse scattering and phase diagram experiments show that Ni-Cu has a clustering (phase segregation) tendency above the observed miscibility gap at 615 K.[40] An earlier SRO calculation[8] reported [000] instability at a spinodal temperature ($\mathrm{T_{sp}}$) of 564 K. We repeated this and also found a $\mathbf{k}_{us} = [000]$ mode at $\mathrm{T_{sp}}$ of 559 K. The KKR-CPA calculation of the $\mathrm{Cu_{50}Ni_{50}}$ solid-solution $\Delta\mathrm{E_f}$ finds +2.90 mRy, a positive value indicating phase segregation with estimated miscibility gap of 660 K. The solid-solution $\Delta\mathrm{E_f}$ and SRO-assessed $\mathrm{T_{sp}}$ indicate segregation on similar energy scale.

A2 Nb-Al-Ti – We apply the new code and analysis to A2 Nb-Al-Ti ternaries, and compare the SRO results and cluster variation method (CVM) calculations by Johnson *et al.*,[12] neutron scattering results by Jacob *et al.*,[41,42] and TEM-ALCHEMI (atom location by channeling enhanced microanalysis) measurements by Fraser *et al.*[43–46] We also found B2-type ordering for Nb-Al-Ti alloys with [111] instability dominated by Ti-Al correlation, arising simply from hybridization and band-filling, as found earlier. The eigenvectors at the instability estimate the occupational probability of each species at different sub-lattices in the ordered structure using (14).

Due to a SRO instability at $\mathbf{k}_{us} = \{111\}$, A2 $\mathrm{NbAlTi_2}$ is unstable to ordering below the order-disorder temper-

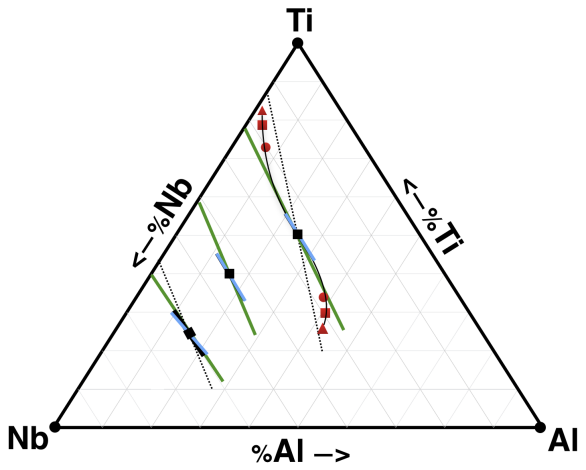

FIG. 2. (color online) For A2 Nb-Al-Ti, concentration-wave polarizations (OTLs) are plotted for lines of short-black (old theory), short-blue (new theory) and green (ALCHEMI[43–46] extended to maximal permitted values). Neutron Rietveld-refinement results[41,42] are plotted by dotted-lines. CVM B2-sublattice concentrations at T/T_c= 0.9, 0.8, 0.7 given by circles, squares, and triangles, respectively.

ature with a concentration wave given by

$$\begin{bmatrix} n^{Nb}(\mathbf{r}) \\ n^{Al}(\mathbf{r}) \end{bmatrix} = \begin{bmatrix} 0.25 \\ 0.25 \end{bmatrix} - \frac{1}{2}\eta(T) \begin{bmatrix} 0.12 \\ 0.81 \end{bmatrix} \times e^{2\pi i(111)\cdot\mathbf{r}} \qquad (19)$$

giving the probability distribution for A2 sites, i.e., cube corner at (000) and center at $\left(\frac{1}{2}\frac{1}{2}\frac{1}{2}\right)$. From (19) the first site probability that vanishes for a given $\eta(T)$ occurs for $n^{Al}(\mathbf{r} = 000)$, giving a maximum LRO of $\eta^{max} = 0.25(0.5 * 0.81)^{-1} = 61.7\%$; it follows that the probability occupation of (Nb, Al, Ti) is (21.3, 0, 78.7)% at cube-corner and (28.7, 50, 21.3)% at cube-center. Clearly, the Nb/Al concentrations are reduced (enhanced) at corner (central) sites, and, as a result, the Ti increases to a maximum of 79% at corners – a partially-ordered B2 structure.

Analytically the ratio of eigenvectors of independent components (with respect to host) at unstable ($\mathbf{k}_{us}$) is

$$\frac{c_{Al}(\frac{1}{2}\frac{1}{2}\frac{1}{2}) - c_{Al}(000)}{c_{Nb}(\frac{1}{2}\frac{1}{2}\frac{1}{2}) - c_{Nb}(000)} = \frac{\mathbf{e}_G^{Al}(\mathbf{k}_{us} = 111)}{\mathbf{e}_G^{Nb}(\mathbf{k}_{us} = 111)} \qquad (20)$$

and, for a ternary, they may be graphically represented by the slope of a line in the Gibbs triangle, Fig. 2, known as ordering-tie-lines (OTLs).[46] Our SRO results compare well with calculated and measured results. The calculated T_{sp} of 1610 K is in good agreement with the measured 1713 K order-disorder.[41]

A1 Cu_2NiZn– Hashimoto *et al.*[47] and Van der Wegen *et al.*[48,49] showed first-order structural transitions from A1 Cu_2NiZn occur at 774 K to a {100}-type partially ordered $L1_2$ structure. Althoff *et al.*[8] predicted {100}-type ordering corresponding to the partially ordered $L1_2$ phase with $T_{sp} = 980\ K$, driven by strong Ni-Zn correlations arising directly from Fermi-surface nesting features, as also found here. With our newly developed analysis approach, we find a similar partially-ordered state at $T_{sp} = 840\ K$. The lower T_{sp} arises from the use of an optimal basis set in KKR-CPA-ASA.

B. High-Entropy Alloy: Al-Co-Cr-Fe-Ni

For HEA formation, Zhang *et al.*[50] proposed three empirical criteria:

1. Mix $N \geq 5$ atoms in near-equiatomic ratio for higher $\Delta S_{pt} = -k_B \sum_i c_i \ln c_i \geq 1.60 k_B$;
2. Have atomic size ratio $\delta < 4.6$ (like Hume-Rothery size effect rule for solid solutions); here, $\delta \equiv \sqrt{\sum_i c_i(1 - r_i/\bar{r})^2}$ for elemental radii r_i and average radii $\bar{r} = \sum_i c_i r_i$;
3. Small $-2.05\delta - 1.94 < \Delta E_f < -0.98\delta + 4.14$ mRy to void compound formation.

Interestingly, so far, many multicomponent system following the above criteria form simple solid-solution phases, e.g., A1, A2 or A3. For AlCoCrFeNi, using an empirical Miedema model by Ren *et al.*[51], we find $\Delta E_f = -1.79$ mRy and $\Delta S_{pt} = 1.61$, so this system obeys the criteria.

Chou *et al.*[52], in their observation for Al-Co-Cr-Fe-Ni, found that increasing %Al plays the role of phase stabilizer. For the readers convenience, we define a parameter Δ (in mole fraction) that controls the Al concentration in $Al_{\frac{\Delta}{5}}\,[CoCrFeNi]_{1-\frac{\Delta}{5}}$. Similar to Chou *et al.*[52] and Zhang *et al.*,[50] we focused our attention to three regions: (1) Al-poor region for $\Delta < 0.5$ with A1 phase; (2) Al-intermediate for $0.5 \leq \Delta < 1.25$, which exhibits a mixed $A1 + A2$ phase; and (3) Al-rich for $1.25 \leq \Delta \leq 2.0$ with A2 phase.[53,54]

We performed KKR-CPA calculations in each region to study relative phase stability (by both VP and ASA methods to assess errors), and then used the KKR-CPA-ASA potentials and charge densities in the SRO calculations (the restriction in the SRO code). We chose one composition within each region: $\Delta = 0.395$ (8%Al) from Al-poor; $\Delta = 1$ (20%Al) from Al-intermediate; and $\Delta = 1.6$ (32%Al) from Al-rich – with equal compensation by remaining elements (Co, Cr, Fe and Ni).

For stability of A2 relative to A1, as shown in Fig. 3, both KKR-CPA VP and ASA results show that that increasing %Al stabilizes the A2 phase in agreement with the experimental observations made by Chou *et al.*[52] and calculations of Zhang *et al.*[57] using CALPHAD (CALculations of PHAse Diagram) techniques.[55,56] The VP results provide a better description of charge and integrations within each VP sites, improving the total energy. (For the ASA, errors in relative phase stability, e.g., A2 versus A1, is a known issue.) The small shift in $E^{A2} - E^{A1}$ from VP versus ASA improves agreement with

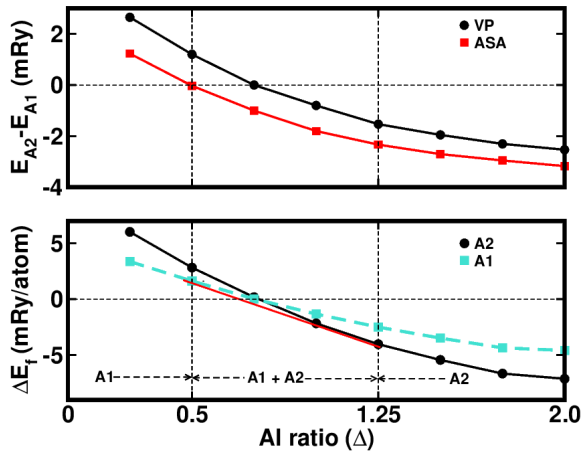

FIG. 3. (color online) For $\mathrm{Al}_{\frac{\Delta}{5}}[\mathrm{CoCrFeNi}]_{1-\frac{\Delta}{5}}$, (Top) Stability of A2 phase relative to A1 phase, for KKR-CPA VP and ASA calculations, see text. (Bottom) Common tangent (solid-red) line to free energy curves shows %Al composition region where mixed A1+A2 phase occurs.

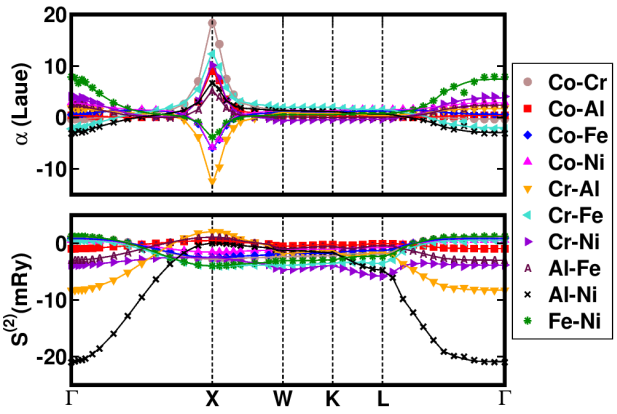

FIG. 4. (color online) For $\Delta = 1.0$ (20% Al) in A1 phase, (upper) $\alpha_{\mu\nu}(\mathbf{k})$ and (lower) $\mathrm{S}^{(2)}_{\mu\nu}(\mathbf{k},\mathrm{T})$ plotted along Γ-X-W-K-L-Γ of the fcc Brilliouin zone.

that measured experimentally, see Fig. 3 (bottom). The common tangents to enthalpy curves shows %Al composition ($0.5 \leq \Delta \leq 1.25$) where two-phase A1+A2 equilibria occurs, which lowers the overall free energy of the homogeneous system into a weighted mix of two phases.

For selected compositions, we performed the linear-response calculations to identify unique SRO modes. We calculated $\mathrm{S}^{(2)}_{\mu\nu}(\mathbf{k},\mathrm{T})$ and determined $\alpha_{\mu\nu}(\mathbf{k})$ for each composition. The $\mathrm{S}^{(2)}_{\mu\nu}(\mathbf{k},\mathrm{T})$ stability matrix is formulated in a "host" picture for mathematical and computational expediency. For ease of interpretation, we convert from host to the "off-diagonal" representation[22] so that the SRO corresponds to all individual pairs directly.

Notably, for binaries, the unstable wavevector in $\alpha(\mathbf{k})$ is same as the favorable modes in $\mathrm{S}^{(2)}(\mathbf{k})$. However, for complex (N > 2) alloys, this need not be the case. Due to the inversion in (6) and intensity conservation (15), the competing eigenvectors in $\mathrm{S}^{(2)}(\mathbf{k})$ can manifest differently in $\alpha(\mathbf{k})$. In this case a careful analysis in real-space can be helpful. In fact, unlike in a binary, a multicomponent alloy can have negative intensity in $\alpha_{\mu\nu}(\mathbf{k})$ relative to homogeneously disordered case, exactly because of this competing nature between modes and intensity conservation. Examples of the effect appear below. In short, in HEA, the instabilities manifest in $\alpha_{\mu\nu}(\mathbf{k})$, may not reflect the pairs driving instability, which shows the importance of present thermodynamic theory.

A1 and A2 equiatomic quinary ($\Delta = 1.0$)

A1 phase– We first focus on the Warren-Cowley SRO parameters[5–7] $\alpha_{\mu\nu}(\mathbf{k})$ (or pair correlations) that may be measured experimentally. The diffuse maximal peaks in Fig. 4 at $\mathbf{k}_{\mathrm{us}} = \{100\}$ (X−points) for $\alpha(\mathbf{k})$ indicates the periodicity of the ordering instabilities in the disordered alloy (not Bragg reflections). At T_{sp}, particular elements of $\alpha(\mathbf{k})$ become unstable (diverge) and indicate second-order instability to LRO. The instability in $\alpha(\mathbf{k})$ is related to the peak in the stability matrix $\mathrm{S}^{(2)}(\mathbf{k})$ in select pairs. The strongest pair in $\mathrm{S}^{(2)}(\mathbf{k})$ driving ordering is Cr−Al, but Co−Cr is the dominant mode in $\alpha(\mathbf{k})$. Clearly, the dominant mode in $\alpha(\mathbf{k})$ is not same as $\mathrm{S}^{(2)}(\mathbf{k})$, but Cr is involved in both competing modes and the strong ordering for one element must be accommodated by the pairs sharing that element.

Just like phonon modes, k-space representation provides relative stability of ordering modes. However, the **k**-space does not necessarily give a direct picture of underlying pair correlations in complex systems. Then, Fourier decomposition of such quantities into real space becomes important. The real-space pair-correlation energies for the select pairs are shown in Table I, which are calculated via Fourier (shell-by-shell) transform

$$S^{(2)}_{\mu\nu}(\mathbf{k}) = S^{(2)}_{\mu\nu,0} + \sum_{i\epsilon n}\sum_{\mu\nu} S^{(2)}_{\mu\nu,n} e^{i\mathbf{k}\cdot\mathbf{R_i}}, \qquad (21)$$

where n represents shell number. Being much larger, Cr−Al pair is a dominant mode. The shell-by-shell calculation gives the strength and spatial extent of $\mathrm{S}^{(2)}(\mathbf{k})$.

The normal modes in Table II are shown at $1.2\mathrm{T}_{\mathrm{sp}}$ ($\mathrm{T}_{\mathrm{sp}} = 448\ K$), which are the eigenvectors of $\mathrm{S}^{(2)}(\mathbf{k})$ driving divergence in SRO. The free energy cost to establish one of these modes vanishes at T_{sp}. Above T_{sp} all eigenvalues remains positive, costing energy to disordered state for substantiating concentration modulations while below T_{sp}, the critical eigenvalue establishes the anticipated probability distribution.

Similar to the $NbAlTi_2$ example, the probability distribution can easily be determined for systems with any

TABLE I. Real-space (21) $S^{(2)}_{\mu\nu,n}$ interchange energies (in mRy) of A1 for $\Delta = 1.0$ for modes Cr−Al, Co−Cr and Cr−Fe.

Shell	Cr−Al	Co−Cr	Cr−Fe
$S^{(2)}_0$	−4.44	+1.91	+2.49
$S^{(2)}_1$	+2.49	−0.68	−0.63
$S^{(2)}_2$	−0.64	−0.13	+0.14
$S^{(2)}_3$	+0.02	+0.16	+0.29
$S^{(2)}_4$	−0.27	+0.28	+0.33

TABLE II. With Ni as host, the normal modes in Gibbs space for A1 AlCoCrFeNi at $1.2T_{sp}$ ($T_{sp} = 448\ K$). $\mathbf{E}_3$ is the mode corresponding to vanishing eigenvalue (highlighted) and used for concentration wave analysis in (14).

Comp.	e_{Al}	e_{Co}	e_{Cr}	e_{Fe}
E_1	+0.15	−1.09	−0.78	−0.20
E_2	+0.83	+0.77	−0.83	−0.08
E_3	−0.21	+0.28	+0.32	−0.60
E_4	+1.11	−0.39	+0.78	−0.03

number of components. Because SRO instability for A1 occurs at star of wavevector $\mathbf{k}_{us} = \{001\}$, i.e., (100), (010) and (001), the system is unstable to ordering into a $L1_2$-like superstructure, where $\gamma = \frac{1}{4}$ by symmetry. The concentration wave is then

$$\begin{bmatrix} n^{Al}(\mathbf{r}) \\ n^{Co}(\mathbf{r}) \\ n^{Cr}(\mathbf{r}) \\ n^{Fe}(\mathbf{r}) \end{bmatrix} = \begin{bmatrix} 0.20 \\ 0.20 \\ 0.20 \\ 0.20 \end{bmatrix} + \frac{1}{4}\eta(T) \begin{bmatrix} -0.21 \\ +0.28 \\ +0.32 \\ -0.60 \end{bmatrix} \times \left[e^{2\pi i(100)\cdot\mathbf{r}} + e^{2\pi i(010)\cdot\mathbf{r}} + e^{2\pi i(001)\cdot\mathbf{r}} \right] \tag{22}$$

gives the probability distribution for A1 sites, i.e., cube corner at (000) and faces at $\{0, \pm\frac{1}{2} \pm \frac{1}{2}\}$. The maximum possible LRO is given by the site probability that vanishes first: Here, that occurs for n^{Fe} at $\mathbf{r} = (000)$ giving $\eta^{max} = 0.2(\frac{3}{4} * 0.6)^{-1} = \frac{4}{9} = 0.44$. Thus, the maximum probability occupation of Al, Co, Cr, Fe, and Ni at cube-corner is 13, 29, 31, 0, and 27%, respectively. Similarly, the occupation at other sites can be evaluated from (22).

A2 phase– At T_{sp} Co−Al and Al−Ni pairs in $\alpha(\mathbf{k})$ become unstable (diverge) and indicate SRO instability in A2 to long-range B2 order, see Fig. 5. Clearly, the instability in $\alpha(\mathbf{k})$ at $\mathbf{k}_{us} = [111]$ is because of Al−Ni peak in stability matrix $S^{(2)}(\mathbf{k})$ indicating ordering tendency of Co−Al and Al−Ni pairs.

For A2 with $\mathbf{k}_{us} = \{111\}$, the system is unstable to a B2 superstructure with $\gamma = \frac{1}{2}$ by symmetry. The concentration wave, corresponding to eigenvector of $S^{(2)}(\mathbf{k})$ driving divergence in SRO, i.e., **E4**, highlighted in Table III, is

$$\begin{bmatrix} n^{Al}(\mathbf{r}) \\ n^{Co}(\mathbf{r}) \\ n^{Cr}(\mathbf{r}) \\ n^{Fe}(\mathbf{r}) \end{bmatrix} = \begin{bmatrix} 0.20 \\ 0.20 \\ 0.20 \\ 0.20 \end{bmatrix} + \frac{1}{2}\eta(T) \begin{bmatrix} +1.20 \\ -0.46 \\ +0.04 \\ -0.27 \end{bmatrix} \times e^{2\pi i(111)\cdot\mathbf{r}} \tag{23}$$

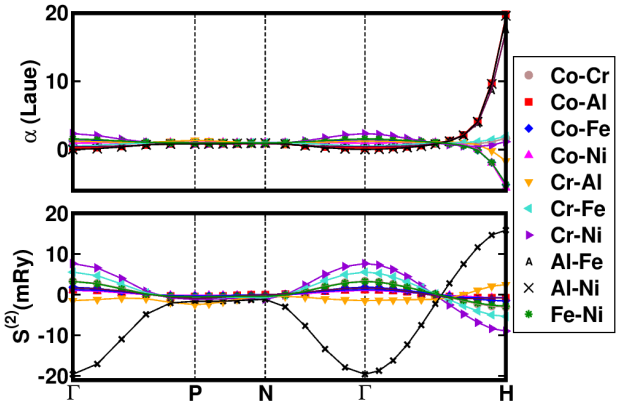

FIG. 5. (color online) For $\Delta = 1.0$ (20% Al) in A2 phase, (upper) $\alpha_{\mu\nu}(\mathbf{k})$ and (lower) $S^{(2)}_{\mu\nu}(\mathbf{k}, T)$ plotted along Γ-P-N-Γ-H of the bcc Brilliouin zone.

giving the probability distribution for A2 sites, i.e., cube corner at (000) and center at $(\frac{1}{2}\frac{1}{2}\frac{1}{2})$. The maximum possible LRO is given by the site probability that vanishes first: here, that occurs for n^{Al} at $\mathbf{r} = (\frac{1}{2}\frac{1}{2}\frac{1}{2})$ giving $\eta^{max} = \frac{1}{3}$. Thus, maximum probability of Al, Co, Cr, Fe and Ni at cube-center is 0, 27.7, 19.3, 24.5 and 28.5%, respectively.

A1 Al-poor quinary ($\Delta = 0.395$)

In Fig. 6, the $\alpha(\mathbf{k})$ instability occurs at $\mathbf{k}_{us} = [000]$ (Γ-point), indicating clustering involving two competing Cr−Al and Cr−Ni pair correlations. Clearly, however, $S^{(2)}(\mathbf{k})$ shows that the strongest exchange energy is in the Cr−Ni pair, which drives clustering and slightly weaker Cr−Al (X-point) ordering energy. This energetics is manifest in $\alpha(\mathbf{k})$ through Cr-based pair correlations (Cr−Al and Cr−Ni) to accommodate favorable $S^{(2)}(\mathbf{k})$ clustering energy in Cr−Ni and weaker ordering energy in Cr−Al, so they are coupled. This effect is driven by the strongest Cr−Ni pair in $S^{(2)}(\mathbf{k})$, but manifest in $\alpha(\mathbf{k})$ in two closely competing modes, i.e., Cr−Al and Cr−Ni.

TABLE III. With Ni as host, the normal modes in Gibbs space for A2 AlCoCrFeNi at $1.2T_{sp}$ ($T_{sp} = 1705\ K$). $\mathbf{E}_4$ is the mode corresponding to vanishing eigenvalue (highlighted) and used for concentration wave analysis in (14).

Comp.	e_{Al}	e_{Co}	e_{Cr}	e_{Fe}
E_1	−0.46	−0.84	−0.99	−0.15
E_2	−0.45	+0.47	+0.22	−0.55
E_3	−0.41	−0.94	+0.98	−0.01
E_4	+1.20	−0.46	+0.04	−0.27

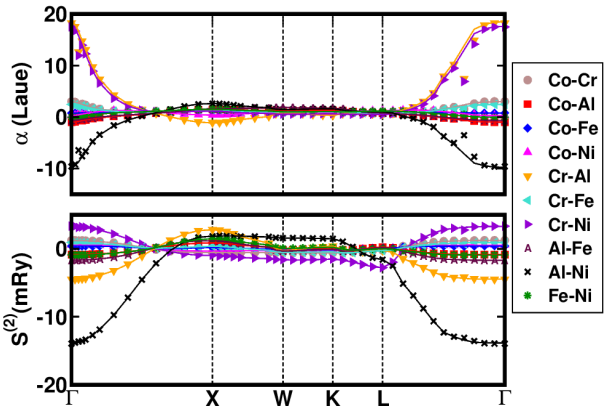

FIG. 6. (color online) For $\Delta = 0.395$ (8% Al) in A1 phase, (upper) $\alpha_{\mu\nu}(\mathrm{k})$ and (lower) $\mathrm{S}^{(2)}_{\mu\nu}(\mathrm{k},\mathrm{T})$ plotted along Γ-X-W-K-L-Γ of the fcc Brilliouin zone.

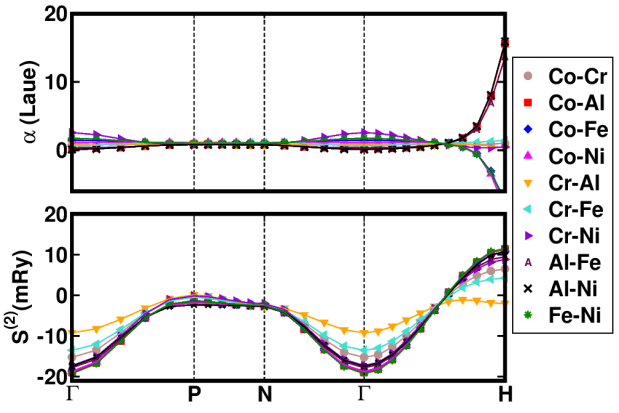

FIG. 7. (color online) For $\Delta = 1.6$ (32% Al) in A2 phase, (upper) $\alpha_{\mu\nu}(\mathbf{k})$ and (lower) $\mathrm{S}^{(2)}_{\mu\nu}(\mathbf{k},\mathrm{T})$ plotted along Γ-P-N-Γ-H of the bcc Brilliouin zone.

A2 Al-rich quinary ($\Delta = 1.6$)

In Fig. 7, the instability in $\alpha(\mathbf{k})$ occurs at $\mathbf{k}_{\mathrm{us}} = [111]$ (H−points) indicating ordering tendency in Al−Ni and Co−Al pairs. However, the peak in $\mathrm{S}^{(2)}(\mathbf{k})$ at H−point is driven by competing pairs Al−Ni, Co−Al and Fe−Ni. Clearly, a small change in pair energies can significantly affect Warren-Cowley parameter.[5–7]

In Al-rich region, the SRO for A2 occurs at $\mathbf{k}_{us} = \{111\}$ indicating an ordering instability to the B2-like superstructure with $\gamma = \frac{1}{2}$ by symmetry. The concentration wave, corresponding to eigenvector of $\mathrm{S}^{(2)}(\mathbf{k})$ driving divergence in SRO, i.e., **E4**, highlighted in Table IV, is

$$\begin{bmatrix} n^{Al}(\mathbf{r}) \\ n^{Co}(\mathbf{r}) \\ n^{Cr}(\mathbf{r}) \\ n^{Fe}(\mathbf{r}) \end{bmatrix} = \begin{bmatrix} 0.32 \\ 0.17 \\ 0.17 \\ 0.17 \end{bmatrix} + \frac{1}{2}\eta(T) \begin{bmatrix} +1.25 \\ -0.48 \\ +0.04 \\ -0.20 \end{bmatrix} \times e^{2\pi i(111)\cdot\mathbf{r}} \qquad (24)$$

giving the probability distribution for A2 sites, i.e., cube corner at (000) and center at $\left(\frac{1}{2}\frac{1}{2}\frac{1}{2}\right)$. The η^{max} is given by the site probability that vanishes first: Here, that occurs for n^{Al} at $\mathbf{r} = \left(\frac{1}{2}\frac{1}{2}\frac{1}{2}\right)$ giving $\eta^{max} = 0.32(\frac{1}{2} * 1.25)^{-1} = 0.512$. Thus, maximum probability occupation of Co, Cr, Fe and Ni at the center is 29.2, 16.0, 22.1 and 32.7%, respectively. Similarly, the occupation at corner site can be evaluated.

TABLE IV. With Ni as host, the normal modes in Gibbs space for Al-rich A2 at $1.2\mathrm{T}_{\mathrm{sp}}$ ($\mathrm{T}_{\mathrm{sp}} = 1190\ K$). $\mathbf{E}_4$ is the mode corresponding to vanishing eigenvalue (highlighted) and used for concentration wave analysis in (14).

Comp.	e_{Al}	e_{Co}	e_{Cr}	e_{Fe}
E_1	−0.40	−0.82	−1.03	−0.15
E_2	−0.32	+0.40	+0.23	−0.58
E_3	−0.41	−0.97	+0.94	−0.02
E_4	+1.25	−0.48	+0.04	−0.20

Electronic Origin of SRO

For better understanding, KKR-CPA density of states results were plotted for $\Delta = 0.395$, 1.0 and 1.6 for A1 and A2 Al-Co-Cr-Fe-Ni systems and tried to connect general behavior to its electronic origin.

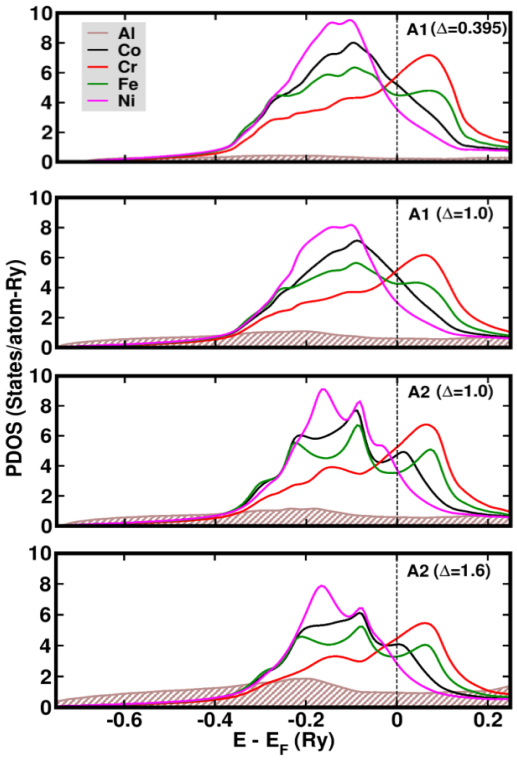

FIG. 8. (color online) For $\mathrm{Al}_{\frac{\Delta}{5}}[\mathrm{CoCrFeNi}]_{1-\frac{\Delta}{5}}$, partial density of states versus energy (relative to E_f) at Δ =0.395, 1.0 and 1.6. For comparison, lattice constant (volume) is kept constant in A1 (6.80 a.u.) and A2 (5.47 a.u.) phases.

In Fig. 8, A2 ($\Delta = 1.0$ and 1.6) has strong hybridized states compared to A1 ($\Delta = 0.395$ and 1.0) which enhances the filling of bonding-type states below E_f, while simultaneously pushing anti-bonding (or non-bonding) states above E_f. But for A1 phase, the disorder broadening leads to weak hybridization, reducing the ordering strength. Clearly, increasing %Al stabilizes the A2 relative to A1, due to increased hybridization in A2 phase resulting in an increased order-disorder temperature.

From our KKR-CPA-ASA, we can compare the ΔE_f and their changes with composition and structure (due to the ASA, trends with Δ and structure can be shifted from full potential results). At $\Delta = 0.395$, the positive $\Delta E_f = +5.19$ mRy for A1 shows clustering nature of the alloy, with an estimated miscibility gap of 523 K. At $\Delta = 1.0$, the negative ΔE_f for A1 (-4.26 mRy) and A2 (-7.66 mRy) shows the ordering nature with estimated order-disorder temperature 679 K and 1217 K, respectively. At $\Delta = 1.6$, negative ΔE_f for A1 (-5.86 mRy) also shows ordering behavior with estimated order-disorder temperature of 932 K. The estimated T_{sp} from SRO calculations are 448 K, 437 K, 1705 K and 1190 K, respectively. The spinodal temperature for A2 increases because of stronger hybridization. Note that, if SRO linear response had charge fluctuations incorporated (i.e. all double counting terms), then Madelung screening, if relevant, can change the magnitude of $S^{(2)}(\mathbf{k})$ and T_{sp}. Here, for the Al-Co-Cr-Fe-Ni systems only hybridization and band-filling are significant in driving ordering or clustering.

VI. CONCLUSION

We have developed an algorithm based on mathematics of $(N-1)$-simplex to analyze uniquely the chemical SRO in N-component solid-solution alloys i.e., thermodynamically induced ordering fluctuations. The eigenvectors associated with the SRO can be interpreted easily within a concentration-wave framework. In addition, we utilized a KKR-CPA based thermodynamic linear-response theory to predict the SRO for N-component solid-solutions described by an inhomogeneous coherent potential approximation. We validated the new SRO code and analysis on experimentally and theoretically well-studied binary and ternary systems. We investigated SRO in quinary Al-Co-Cr-Fe-Ni systems using new approach in three regions with different %Al, that is, Al-poor with $\Delta < 0.5$, Al-intermediate with $0.5 \leq \Delta \leq 1.25$ and Al-rich with $1.25 < \Delta \leq 2.0$, all of which show simple solid-solution phases, i.e., A1, A2 or both. The thermodynamic predictions from our electronic-structure-based theories of formation energy and short-range order from linear-response agree with all known measurements. Given that SRO is difficult to measure in HEA alloys, and has yet to be attempted, our validated theory provides predictive methods to guide experiment and to assess properties for design of complex alloy systems.

For future design purposes, we propose to combine SRO prediction over the entire Gibbs space with structural stability (A1 versus A2 versus A3) and mechanical property estimates using stacking fault energy to narrow the search space for desired chemical and mechanical behavior. Notably, stacking fault calculations must include the Suzuki effect,[58,59] where solute is attracted (repelled) from the defect to lower (maintain) the defect energy, or otherwise the mechanical strength can be highly overestimated.[60]

VII. ACKNOWLEDGMENTS

We would like to thank Bob Haber (University of Illinois Urbana-Champaign) for useful discussions on barycentric coordinates, and Frank Pinski (University of Cincinnati) on helping resurrect elements of our old SRO code during his visit last summer. The work was supported by the U.S. Department of Energy (DOE), Office of Science, Basic Energy Sciences, Materials Science and Engineering Division. The research was performed at the Ames Laboratory, which is operated for the U.S. DOE by Iowa State University under contract No. DE-AC02-07CH11358.

Appendix: Cartesian Representation of Regular Simplices in arbitrary dimension: an (N-1)-simplex

In geometry, triangle or higher-order polygon can be generalized into a polytope of arbitrary dimension, also known as simplex.[61] A $(N-1)$-simplex is defined as a geometric object that has N-vertices and $N(N-1)/2$ edges. By convention, a $(N-1)$-simplex has N-barycentric coordinates defined to all sum to one, and, as such, the N^{th}-coordinate is redundant (linearly dependent).

A regular $(N-1)$-simplex is a polygon with equal edge lengths and N-vertices, so compositions $\{c_i\}$ of constituents in an N-component alloy are natural barycentric coordinates with c_N a dependent variable, as to be used in a "host" picture. For a ternary system, for example, the Gibbs (equilateral) triangle in composition space uniquely describes compositions of the alloy along its edges, see Fig. 2. Here, three pure components are represented by three corners.

To introduce barycentric coordinates, we consider a case of 2-simplex, Fig. 9, represented by a ternary Gibbs triangle. The point P is an arbitrary barycentric point in 2-simplex S with vertices A_i ($i = 1-3$). With this definition, we can construct N edges between P and the 3 vertices A_i to define 3 simplexes S_i covering S. Opposing each vertex A_i of the 2-simplex are smaller 2-simplices S_i with N_i edges. The barycentric coordinates of point P are (B_1, B_2, B_3). With this, we can generalize to (N-1)-

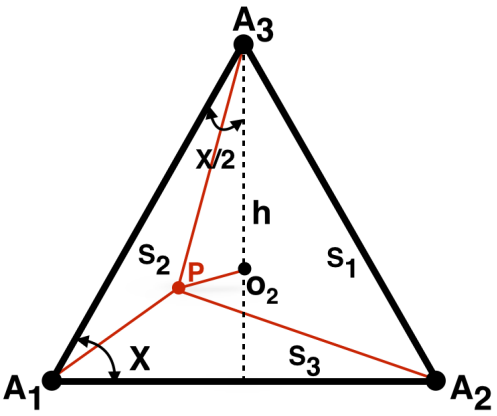

FIG. 9. Height h of triangle $\Delta A_1A_2A_3$ can be generalized to evaluate the height of regular polygon, here, $(N-1)$-simplex. P-O_2 is shift from composition to centroid of the simplex.

simplex with N edges between P and N vertices A_i to define N (N-1)-simplexes S_i covering S. The barycentric coordinate of point P in (N-1)-simplex, (B_1, B_2,$\cdots$, B_N), found to be

$$B_i = \frac{area(S_i)}{area(S)} \equiv c_i. \qquad (A.1)$$

It is self-evident by definition that $\sum_{i=1}^{N} B_i = 1$ and independent of point P; hence, compositions $\{c_i\}$ are the natural barycentric coordinates for the alloy problem. This relation also gives the coordinates of redundant vertex N. Each vertex of S represents a single component of the alloy, so it has value '1' and all remaining components will be '0'. For example, in Fig. 9, the centroid 'o_2', and the three vertices A_1, A_2, and A_3 have barycentric coordinates $(1/3, 1/3, 1/3)$ and $(1, 0, 0)$, $(0, 1, 0)$, $(0, 0, 1)$, respectively.

The transformation matrix $^{N\text{-}1}$T to go from orthogonal to oblique coordinates is straightforward for any dimension, where rank (N-1) of the matrix increases with the order of simplex. Generally, from finite-element (arbitary simplices) T is that given in the main text (10). What remains is to derive analytically the matrix elements $\{X_i^j\}$, which are scaled by the height of (N-1)-simplex with respect to host (N^{th} vertex).

An analytical form for T enables the direct transform of N-component orthogonal eigenvectors to oblique compositional ones for proper chemical interpretation. The final Gibbs' eigenvectors describe properly the physical SRO concentration waves. The elements of the transformation matrix are calculated analytically in two steps.

1. General formula for the height of N-simplex

First, we consider 2-simplex, i.e. equilateral triangle, with $A_1A_2 = A_2A_3 = A_3A_1 = 1$ (unit length), see Fig. 9. The height of such a triangle is $h = \cos\frac{X}{2}$. Angle $X = \angle A_2A_1A_3$ is the dihedral angle of the regular 2-simplex and defined by scalar product, $\overline{A_1A_2} \cdot \overline{A_1A_3} = \cos X = \frac{1}{2}$, which results in $h = \sqrt{\frac{1}{2}(1+\cos X)} = \frac{\sqrt{3}}{2}$.

The relation between the height of a regular (N-1)-simplex and its dihedral angle is the same as for 2-simplex

$$h = \cos\frac{X}{2} = \sqrt{\frac{1}{2}[1+\cos X]} = \sqrt{\frac{N}{2(N\text{-}1)}}. \qquad (A.2)$$

Here, we use the elementary result for the dihedral angle,[63] i.e., $\cos X = (N\text{-}1)^{-1}$.

2. Cartesian coordinates of vertices of N-simplex

In $(N-1)$-simplex, the Cartesian coordinates of each vertex A_N with respect to centroid 'o_{N-1}' can be determined with following conditions:

1. For a regular simplex, the distances of each vertex from center will be a constant.

2. The scalar product of two vertices of $(N-1)$-simplex with respect to its center $(\frac{1}{N-1}, \frac{1}{N-1}, \cdots, \frac{1}{N-1})$ will give the angle subtended, i.e., $arccos\left[-(N-1)^{-1}\right]$.[62,63]

here, in Fig. 9, A_1, A_2 and A_3 are equidistant vertices with length 'a' from centroid 'o_2' and angle subtended is $arccos\left[-\frac{1}{2}\right]$.

In a host picture for a N-component alloy, the T matrix is rank $(N-1)$ and must be evaluated with respect to N^{th} vertex of regular $(N-1)$-simplex. Here, the coordinate of all vertices are known in terms of center as the origin, so we translate the origin from center to the N^{th} vertex. Next, the vertex coordinates are scaled by the height of $(N-1)$-simplex calculated analytically, i.e., $\sqrt{N/2(N-1)}$. This cumulative result can be used for any alloy without change.

It follows that the coordinates of $(N-1)$ vertices are analytically given by the relation (11)

$$X_i^j - X_i^N = -\frac{1}{X_i^i}\sqrt{\frac{2(N-1)}{N}}\left[\mathbf{X}_{i-1}^i \cdot \mathbf{X}_{i-1}^j + \frac{1}{N-1}\right],$$

where each i, j runs from 1 to $N-1$. For example, T for binary (12), quaternary, and quinary (13) are given in the text. This T matrix for N-component alloy ensures that the Gibbs' eigenvectors, after transformation, are both algebraically and geometrically orthogonal (see main text). This transformation is used to determine eigenvectors, SRO and concentration waves, and guarantees that $0 \le c_\mu \le 1$.

* prashant@ameslab.gov
† smirnov@ameslab.gov
‡ ddj@ameslab.gov

[1] J. W. Yeh, S. K. Chen, S. J. Lin, J. Y. Gan, T. S. Chin, T. T. Shun, C. H. Tsau, and S. Y. Chang, Nanostructured High-Entropy Alloys with Multiple Principal Elements: Novel Alloy Design Concepts and Outcomes, Adv. Eng. Mater. **6**. 299 (2004).
[2] J. W. Yeh, Alloy Design Strategies and Future Trends in High-Entropy Alloys, Ann. Chim-Sci Mat. **31**, 633 (2006).
[3] J. D. Althoff, D. D. Johnson, F. J. Pinski, and J. B. Staunton, Electronic origins of ordering in multicomponent metallic alloys: Application to the Cu-Ni-Zn system, Phys. Rev. B **53**, 10610 (1996).
[4] J. D. Althoff and D. D. Johnson, Concentration-wave analysis of atomic pair correlations disordered ternary alloys: Application to Cu_2NiZn, Computational Materials Science **8**, 71 (1997).
[5] J. M. Cowley, An Approximate Theory of Order in Alloys, Phys. Rev. 77, 669 (1950)
[6] B. E. Warren, *X-ray Diffraction*, (Addison-Wesley, Reading, Massachusetts, 1969).
[7] J.M. Cowley, *Diffraction Physics*, (Elsevier, Amsterdam, 1975).
[8] J. D. Althoff, D. D. Johnson, and F. J. Pinski, Commensurate and Incommensurate Ordering Tendencies in the Ternary fcc Cu-Ni-Zn System, Phys. Rev.Lett. **74**, 138 (1995).
[9] D. D. Johnson, Computation of Diffuse Intensities in Alloys, in *Characterization of Materials* edited by E.N. Kaufmann (John Wiley and Sons, Inc. 2012) p. 1-31.
[10] J. B. Staunton, D. D. Johnson, and F. J. Pinski, Compositional short-range ordering in metallic alloys: Band-filling, charge-transfer, and size effects from a first-principles all-electron Landau-type theory, Phys. Rev. B **50**, 1450 (1994).
[11] D. D. Johnson, J. B. Staunton, and F. J. Pinski, First-principles all-electron theory of atomic short-range ordering in metallic alloys: $D0_{22}-$ versus $L1_2-$like correlations, Phys. Rev. B **50**, 1473 (1994).
[12] D. D. Johnson, M. Asta, and J. D. Althoff, Temperature-dependent chemical ordering in bcc-based ternary alloys: A theoretical study of Ti-Al-Nb, Philosophical Magazine Letters **79**, 551 (1999).
[13] A. Khatcharuryan, *Theory of Structural Transformation in Solids* (Wiley, New York, 1983).
[14] M. Krivoglaz, *Theory of X-ray and Thermal-Neutron Scattering by Real Crystals*, (Plenum Press New York) (1969).
[15] P. C. Clapp and S. C. Moss, Correlation Functions of Disordered Binary Alloys. I, Phys. Rev. **142**, 418 (1996).
[16] F. Ducastelle, *Order and phase stability in alloys*, edited by F. de Boer and D. Pettifor, North Holland. Amsterdam, the Netherlands, p. 308 (1991).
[17] R. Evans, The nature of the liquid-vapour interface and other topics in the statistical mechanics of non-uniform, classical fluids, Advances in Physics **28**, 143 (1979).
[18] B. L. Györffy and G. M. Stocks, Concentration Waves and Fermi Surfaces in Random Metallic Alloys, Phys. Rev.Lett. **50**, 374 (1983).
[19] B. L. Györffy *et al.*, in Alloy Phase Stability, edited by G. M. Stocks and A. Gonis (Kluwer, Dordrecht, 1989), p. 421.
[20] J. B. Staunton, D. D. Johnson, and F. J. Pinski, Theory of compositional and magnetic correlations in alloys: Interpretation of a diffuse neutron-scattering experiment on an iron-vanadium single crystal, Phys. Rev.Lett. **65**, 1259 (1990).
[21] Abraham Ungar, *Barycentric Calculus In Euclidean And Hyperbolic Geometry: A Comparative Introduction*, (World Scientific, New Jersey, 2010).
[22] D. de Fontaine, An analysis of clustering and ordering in multicomponent solid solutions-II fluctuations and kinetics, J. Phys. Chem. Solids **34**, 1285 (1973).
[23] D. de Fontaine, *Solid State Physics: Advances in Research and Applications*, edited by D. Turnbull, F. Seitz, and H. Ehrenreich (Academic, New York, 1979), Vol. **34**, p. 73.
[24] D. D. Johnson, A. V. Smirnov, and S. N. Khan *MECCA: Multiple-scattering Electronic-structure Calculations for Complex Alloys (KKR-CPA Program, ver. 2.0)* (Iowa State University and Ames Laboratory, 2015).
[25] D. D. Johnson, D. M. Nicholson, F. J. Pinski, B. L. Gyorffy, and G. M. Stocks, Density-Functional Theory for Random Alloys: Total Energy within the Coherent-Potential Approximation, Phys. Rev.Lett. **56**, 2088 (1986); Total-energy and pressure calculations for random substitutional alloys, Phys. Rev. **B 41**, 9701 (1990).
[26] D. D. Johnson and F. J. Pinski, Inclusion of charge correlations in calculations of the energetics and electronic structure for random substitutional alloys, Phys. Rev. B **48**, 11553 (1993).
[27] Aftab Alam, S. N. Khan, Brian G. Wilson and D. D. Johnson, Efficient isoparametric integration over arbitrary space-filling Voronoi polyhedra for electronic structure calculations, Phys. Rev. B **84**, 045105 (2011).
[28] H. J. Monkhorst and J. D. Pack, Special points for Brillouin-zone integrations, Phys. Rev. B **13**, 5188 (1976).
[29] U. Von Barth and L. Hedin, A local exchange-correlation potential for the spin polarized case. i, J. Phys. C : Solid State Phys. **5**, 1629 (1972).
[30] V. L. Moruzzi, J. F. Janak and A. R. Williams, *Calculated Electronic Properties of Materials* (Pergamon Press Inc., New York 1978).
[31] Aftab Alam, Suffian N. Khan, A. V. Smirnov, D.M. Nicholson, and D. D. Johnson, Green's function multiple-scattering theory with a truncated basis set: An augmented-KKR formalism, Phys. Rev. B **90**, 205102 (2014).
[32] Aftab Alam and D. D. Johnson, Structural properties and relative stability of (meta)stable ordered, partially ordered, and disordered Al-Li alloy phases, Phys. Rev. B **85**, 144202 (2012).
[33] D. D. Johnson, Modified Broyden's method for accelerating convergence in self-consistent calculations, Phys. Rev. B **38**, 12807 (1988).
[34] F. J. Pinski, J. B. Staunton, and D. D. Johnson, Charge-correlation effects in calculations of atomic short-range order in metallic alloys, Phys. Rev. B **57**, 15177 (1998).
[35] L. Onsager, Electric Moments of Molecules in Liquids, J. Am. Chem. Soc. **58**, 1468 (1936).
[36] Teck L. Tan, and and D. D. Johnson, Topologically correct phase boundaries and transition temperatures for Ising Hamiltonians via self-consistent coarse-grained cluster-lattice models, Phys. Rev. B **83**, 144427 (2011).

[37] F. J. Pinski, B. Ginatempo, D. D. Johnson, J. B. Staunton, G. M. Stocks, and B. L. Gyorffy, Origins of compositional order in NiPt alloys, Phys. Rev.Lett. **66**, 766 (1991).

[38] J. F. Clark, F. J. Pinski, D. D. Johnson, P. A. Sterne, J. B. Staunton, and B. Ginatempo, van Hove Singularity Induced $L1_1$ Ordering in CuPt, Phys. Rev.Lett. **74**, 3225 (1995).

[39] Aftab Alam, Brent Kraczek, and D.D. Johnson, Structural, magnetic, and defect properties of Co-Pt-type magnetic-storage alloys: Density-functional theory study of thermal processing effects, Phys. Rev. B **82**, 024435-16 (2010).

[40] J. Vrijen and S. Radelaar, Clustering in Cu-Ni alloys: A diffuse neutron-scattering study, Phys. Rev. B **17**, 409 (1978).

[41] V. Jacob, C. Colinet, P. Desre, and F. Moret, Calcul de la limite de phases A2/B2 dans le systme Nb-Ti-Al par la mthode variationnelle des amas, J. Phys. (France) **6**, C2-3 (1996).

[42] V. Jacob, PhD thesis, Institut National Polytechnique de Grenoble, France (1996).

[43] D. Banerjee, T. K. Nandi, and A. K. Gogia, Site occupation in the ordered beta phase of ternary Ti-Al-Nb alloys, Scripta metall. **21**, 597 (1987).

[44] W. D. Qian, J. C. H. Spence, M. Kuwabara, and R. Strychor, Least-squares axial alchemi for Nb site determination in a TiAl intermetallic alloy, Scripta metall. **25**, 337 (1991).

[45] T. Sikora, G. Hug, M. Jaoe, and A. M. Flank, *Proceedings of the 38th Colloquium on Metallography*, Saclay, France, Editions de Physique, Journal de Physique *IV*, Vol. **6**, p. 15 (1996).

[46] D.H. Hou and H.L. Fraser, The ordering scheme in Nb aluminides with the B2 crystal structure, Scripta materialia, **36**, 617 (1997).

[47] S. Hashimoto, H. Iwasaki, K. Ohshima, J. Harada, M. Sakata, and H. Terauchi, Study of Local Atomic Order in a Ternary $Cu_{0.47}Ni_{0.29}Zn_{0.24}$ Alloy Using Anomalous Scattering of Synchrotron Radiation, J. Phys. Soc. Jpn. **54**, 3796 (1985).

[48] G. J. L. Van de Wegen, A. De Rooy, P.M. Bronsveld, and J.Th.M. De Hosson, The Order-Disorder Transition in the Quasi-binary cross section $Cu_{50}Ni_{50-x}Zn_x$, Scr. Metall. **15**, 1359 (1981).

[49] A. De Rooy, G. J. L. Van Der Wegen, P. M. Bronsveld, and J.Th.M. De Hosson, The quasi-binary cross section in the ternary system CuNiZn: II. Electrical Resistivity Measurements, Scr. Metall. **15**, 1362 (1981).

[50] Y. Zhang and Y.J. Zhou, Solid Solution Formation Criteria for High Entropy Alloys, Mater. Sci. Forum **561**, 1731 (2007).

[51] Ming-xing Ren, Band-sheng Li, and Heng-zhi Fu, Formation condition of solid solution type high-entropy alloy, Tras. Nonferrous Met. Soc. China **23**, 991 (2013).

[52] H. P. Chou, Y. S. Chang, S. K. Chen, and J. W. Yeh, Microstructure, thermophysical and electrical properties in Al_xCoCrFeNi ($0 \leq x \leq 2$) high-entropy alloys, Mater Sci Eng B Adv. Funct. Solid-State Mater. **163 (3)**, 184 (2009).

[53] C. J. Tong, Y. L. Chen, J. W. Yeh, S. J. Lin, S. K. Chen, T. T. Shun, C. H. Tsau, and S. Y. Chang, Microstructure characterization of Al_xCoCrCuFeNi high-entropy alloy system with multiprincipal elements, Metall. Mater. Trans. A **36 (4)**, 881 (2005).

[54] Y.F. Kao, S.K. Chen, T.J. Chen, P.C. Chu, J.W. Yeh and, S.J. Li, Electrical, magnetic, and Hall properties of Al_xCoCrFeNi high-entropy alloys, J. Alloy Compd. **509 (5)**, 1607 (2011).

[55] L. Kaufman and H. Bernstein, *Computer Calculation of Phase Diagrams*, (Academic Press New York, 1970).

[56] N. Saunders and P. Miodownik, *CALPHAD (Calculation of Phase Diagrams): A Comprehensive Guide* **Vol 1**, edited by R. W. Cahn, (Pergamon Materials Series, 1998).

[57] C. Zhang, F. Zhang, S. Chenn, and W. Cao, Computational Thermodynamics Aided High-Entropy Alloy Design, The Journal of The Minerals, Metals and Materials Society **64**, 839 (2012).

[58] H. Suzuki, Sci. Repts. Tohoku Univ. **A4**, 455 (1952).

[59] H. Suzuki, Segregation of Solute Atoms to Stacking Faults, J. Phys. Soc. (Japan) **17**, 322 (1962).

[60] D. Finkenstadt and D. D. Johnson, Solute/defect-mediated pathway for rapid nanoprecipitation in solid solutions: Γ surface analysis in fcc Al-Ag, Phys. Rev. B **73**, 024101 (2006).

[61] E. L. Elte, *The Semiregular Polytopes of the Hyperspaces*, Groningen: University of Groningen Chapter IV, five dimensional semiregular (1912).

[62] W. Krasnodebski, *Dihedral angle of the regular n-simplex*, Commentationes Mathematicae, Prace Matematyczne **15**, 87 (1971).

[63] H. R. Parks and D. C. Wills, An elementary calculation of the dihedral angle of the regular n-simplex, American Mathematical Monthly **109 (8)**, 756 (2002).